






Direct Estimates of the Solar Coronal Magnetic Field Using Contemporaneous Extreme-ultraviolet, Radio, and White-light Observations

Anshu Kumari¹ , R. Ramesh¹, C. Kathiravan¹, T. J. Wang^{2,3} , and N. Gopalswamy³ 

¹Indian Institute of Astrophysics, 100 Feet Road, Koramangala II Block, Bangalore, Karnataka—560034, India

²Department of Physics, The Catholic University of America, Washington, DC 20064, USA

³NASA Goddard Space Flight Center, Code 671, Greenbelt, MD 20771, USA

Received 2019 March 8; revised 2019 June 12; accepted 2019 June 14; published 2019 August 8

Abstract

We report a solar coronal split-band type II radio burst that was observed on 2016 March 16 with the Gauribidanur Radio Spectro-Polarimeter in the frequency range $\approx 90\text{--}50$ MHz, and the Gauribidanur Radioheliograph at two discrete frequencies, viz. 80 and 53.3 MHz. Observations around the same epoch in extreme ultraviolet (EUV) and white light show that the above burst was associated with a flux-rope structure and a coronal mass ejection (CME), respectively. The combined height–time plot generated using EUV, radio, and white-light data suggests that the different observed features (i.e., the flux rope, type II burst, and the CME) are all closely associated. We constructed an empirical model for the coronal electron density distribution ($N_e(r)$, where r is the heliocentric distance) from the above set of observations themselves and used it to estimate the coronal magnetic field strength (B) over the range of r values in which the respective events were observed. The B values are consistent with each other. They vary as $B(r) = 2.61 \times r^{-2.21}$ G in the range $r \approx 1.1\text{--}2.2R_\odot$. As far as we know, similar direct estimates of B in the near-Sun corona without assuming a model for $N_e(r)$, and by combining cotemporal set of observations in two different regions (radio and white-light) of the electromagnetic spectrum, have rarely been reported. Further, the present work is a novel attempt where the characteristics of a propagating EUV flux-rope structure, considered to be the signature of a CME close to the Sun, have been used to estimate $B(r)$ in the corresponding distance range.

Key words: Sun: activity – Sun: corona – Sun: coronal mass ejections (CMEs) – Sun: magnetic fields – Sun: radio radiation

1. Introduction

The formation, evolution, and characteristics of coronal mass ejections (CMEs), coronal streamers, coronal holes, and coronal loops in the solar atmosphere are primarily determined by the coronal magnetic field. But measurements of the solar coronal magnetic field are presently limited due to practical difficulties (see, e.g., Lin et al. 2000; Tomczyk et al. 2008). It is inferred by extrapolating the observed solar surface magnetic field distribution using the potential or force-free field approximations (see, e.g., Wiegmann et al. 2017 for a recent review on the subject). Estimates of the coronal magnetic field strengths, particularly in the middle corona ($r \approx 1.1\text{--}3.0R_\odot$), are largely obtained using observations of either the circularly polarized radio emission (i.e., the Stokes V emission) from the transient low-frequency ($\lesssim 150$ MHz) radio events like the type I, II, III, IV, and V bursts, or the split-band feature exhibited by some of the radio type II bursts (Smerd et al. 1975; Dulk & McLean 1978; Dulk & Suzuki 1980; Gopalswamy et al. 1986; Bastian et al. 2001; Vrřnak et al. 2002; Mancuso et al. 2003; Ramesh et al. 2003, 2004, 2011, 2013; Cho et al. 2007; Zimovets et al. 2012; Mancuso & Garzelli 2013; Sasikumar Raja & Ramesh 2013b; Tun & Vourlidis 2013; Hariharan et al. 2014; Sasikumar Raja et al. 2014; Zucca et al. 2014b; Kishore et al. 2016, 2017). Weak circularly polarized components in the thermal radio emission from discrete sources at low frequencies (Sastri 2009; Ramesh et al. 2010b) and geometrical properties of the propagating disturbances observed in extreme-ultraviolet (EUV) images of the solar atmosphere (Gopalswamy et al. 2012) have also been used to estimate coronal magnetic strength. Kwon et al. (2013) carried out global coronal

seismology from the propagation speed of a fast magnetosonic wave to determine $B(r)$ in the extended corona. Despite all these different measurements, a combined estimate of $B(r)$ using observations in the different regions of the electromagnetic spectrum and particularly close to the Sun are very limited (Dulk & McLean 1978; Vrřnak et al. 2002; Mancuso et al. 2003, 2019; Cho et al. 2007; Zimovets et al. 2012; Zucca et al. 2014b; Kumari et al. 2017b, 2017c). Equally rare are reports where the same set of observations are used to independently derive the coronal electron density ($N_e(r)$) required to estimate $B(r)$. This is important since $B(r)$ will be otherwise sensitive to the density model used (see, e.g., Vrřnak et al. 2002).

In the present work we take advantage of the simultaneous imaging and spectropolarimetric observations of a type II radio burst with the ground-based facilities and EUV, white-light observations of the solar corona with instruments on board space platforms to estimate $B(r)$ in the distance range $r \approx 1.1\text{--}2.2R_\odot$. The paper is arranged as follows: In Section 2, we have reported the observations and the related instruments. The data analysis and results are discussed in Section 3 with a summary given in Section 4.

2. Observations

2.1. Radio Observations

The radio observations reported in the present work were carried out using the different facilities operated by the Indian Institute of Astrophysics (IIA) in the Gauribidanur

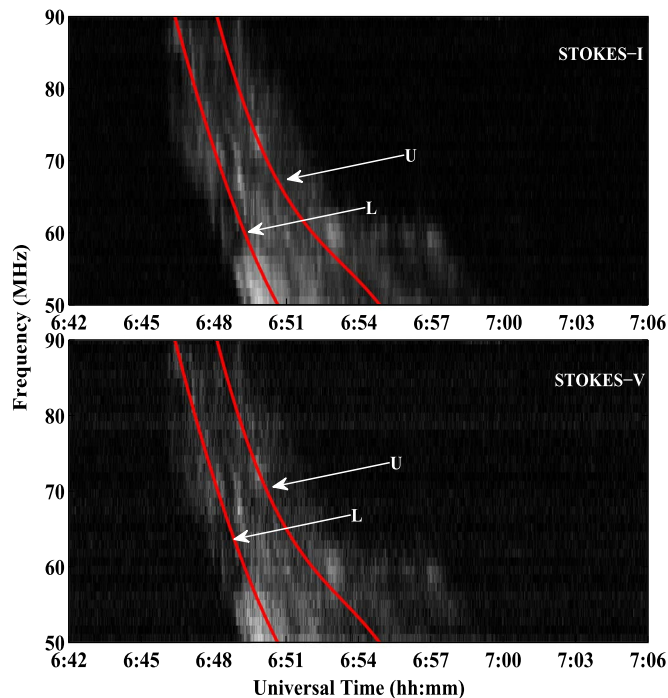


Figure 1. Dynamic spectra of the split-band type II radio burst observed with the GRASP on 2016 March 16 during the time interval $\approx 06:45\text{--}07:00$ UT. The red lines indicate the lower (*L*) and upper (*U*) bands of the burst.

Observatory⁴ (Ramesh 2011). The Gauribidanur Radio Spectro-Polarimeter (GRASP; Hariharan et al. 2015; Kishore et al. 2015) observed a split-band type II radio burst from the Sun on 2016 March 16 during the period $\approx 06:45\text{--}07:00$ UT. The frequency range of the burst was $\approx 90\text{--}50$ MHz. Figure 1 shows the dynamic spectra of the burst observed with the GRASP in Stokes *I* and *V*. Radio frequency interference in the observations is minimal (Monstein et al. 2007). The estimated peak degree of circular polarization (dcp) is in the range $\approx 8\%\text{--}11\%$. The durations of the lower (*L*) and upper (*U*) bands of the split-band burst at a typical frequency like 88 MHz are ≈ 2.3 minutes and ≈ 2.5 minutes, respectively (see Figure 2). The half-power width of the response pattern of GRASP is $\approx 90^\circ \times 60^\circ$ (R.A. \times decl.) and is nearly independent of frequency. The primary receiving element used in GRASP is a Crossed Log-Periodic Dipole (Sasikumar Raja et al. 2013a). The integration time is ≈ 250 ms, and the observing bandwidth is ≈ 1 MHz at each frequency. The antenna and the receiver systems were calibrated by carrying out observations in the direction of the Galactic center as described in Kishore et al. (2015). The burst was observed elsewhere also⁵ including the Gauribidanur Radio Interferometer Polarimeter (Ramesh et al. 2008), the Gauribidanur LOw-frequency Solar Spectrograph (GLOSS; Ebenezer et al. 2001, 2007; Kishore et al. 2014), and e-Callisto (Benz et al. 2009) in Gauribidanur⁶ and Ooty⁷. It was associated with a C2.2 class soft X-ray (SXR) flare observed with the *Geostationary Operational Environmental Satellite* (GOES-15) from the NOAA sunspot

⁴ <https://www.iiap.res.in/?q=centers/radio>

⁵ <ftp://ftp.swpc.noaa.gov/pub/warehouse/2016/>

⁶ http://soleil.i4ds.ch/solarradio/qkl/2016/03/16/GAURI_20160316_064459_59.fit.gz.png

⁷ http://soleil.i4ds.ch/solarradio/qkl/2016/03/16/OOTY_20160316_064443_59.fit.gz.png

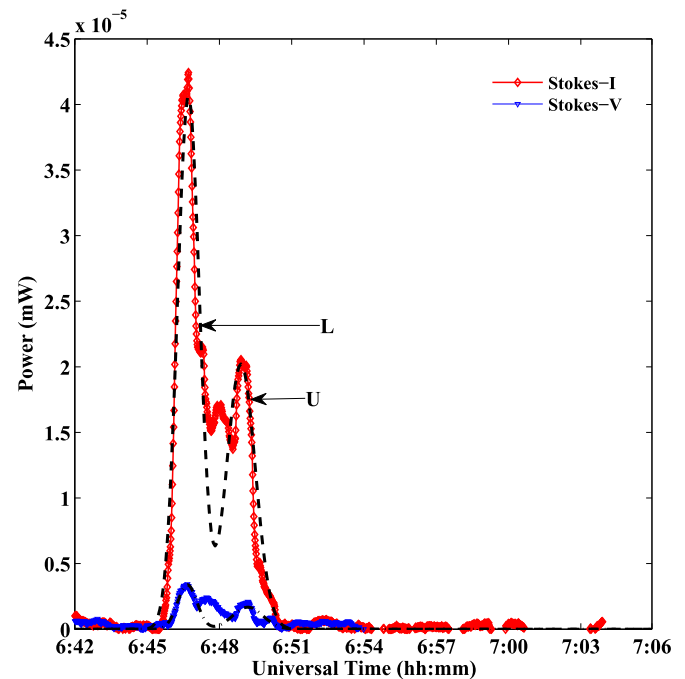


Figure 2. Temporal profile of the split-band type II burst in Figure 1 around 88 MHz, averaged over a bandwidth of ≈ 4 MHz. The dotted lines represent Gaussian fits to the observed profiles.

active region AR12522 located at the heliographic coordinates N12W83.⁸ The above flare was present in the time interval $\approx 06:34\text{--}06:57$ UT, with peak at $\approx 06:46$ UT. The location of the split-band burst in the solar atmosphere was inferred from observations with the Gauribidanur Radioheliograph (GRAPH; Ramesh et al. 1998, 1999a, 2006b) at 80 and 53.3 MHz (see Figure 5). The GRAPH is a T-shaped radio interferometer array that produces two-dimensional images of the solar corona with an angular resolution of $\approx 5' \times 7'$ (R.A. \times decl.) at a typical frequency like 80 MHz. The integration time is ≈ 250 ms and the observing bandwidth is ≈ 2 MHz. We would like to add here that both the type II bursts shown in Figure 5 correspond to the lower (*L*) band of the split-band type II burst in Figure 1.

2.2. Optical Observations

The optical data reported in the present work were obtained in EUV at 211 Å with the Atmospheric Imaging Assembly (AIA; Lemen et al. 2012) on board the *Solar Dynamics Observatory* (SDO), and in white light with the COR1 coronagraph of the Sun-Earth Connection Coronal and Heliospheric Investigation (Howard et al. 2008) on board the *Solar Terrestrial Relationship Observatory* (STEREO)⁹ and the Large Angle and Spectrometric Coronagraph (LASCO; Brueckner et al. 1995) on board the *Solar and Heliospheric Observatory* (SOHO). The STEREO-A/COR1 instrument observed a CME around the same time as the type II burst in Figure 1. The CME was first seen in the STEREO-A/COR1 field of view (FOV) at $\approx 06:50$ UT and was noticeable until $\approx 07:05$ UT (see Figure 3). The projected heliocentric distance of the centroid of the CME (r_{CME}) during its first appearance was $1.66R_{\odot}$. The angular width of the CME was $\approx 36^\circ$. The

⁸ <https://www.solarmonitor.org/index.php?date=20160316>

⁹ <https://cor1.gsfc.nasa.gov/>

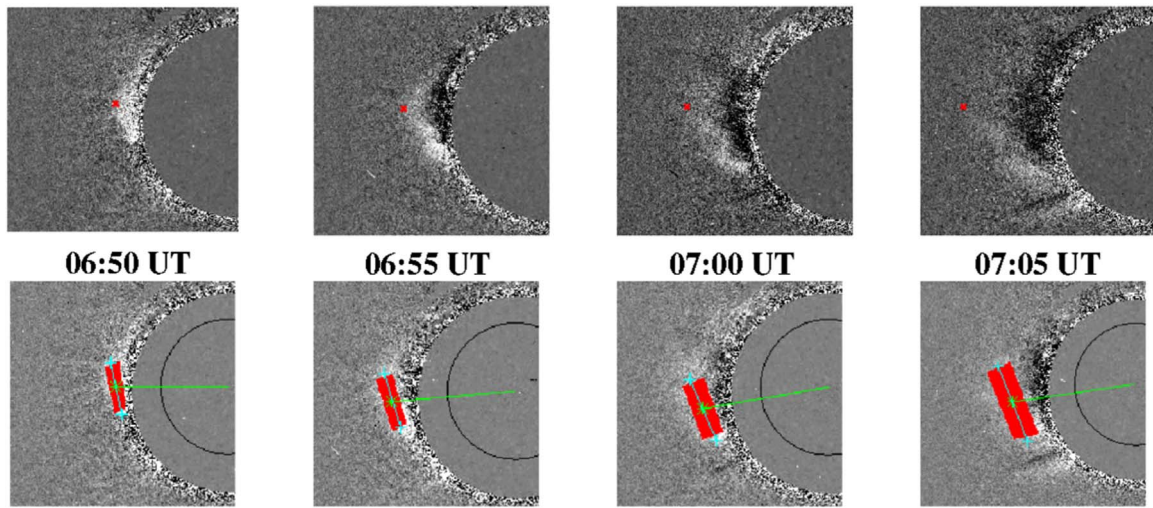


Figure 3. Upper panels: *STEREO-A/COR1* polarized brightness (pB) difference images of the CME that was observed on 2016 March 16 between $\approx 06:50$ and $\approx 07:05$ UT. The red cross marks indicate the LE of the CME at different epochs. The gray circle represents the coronagraph occulter (radius $\approx 1.4R_{\odot}$). Lower panels: same as the upper panels, but with a marking of the CME region (indicated by the red box) used for estimating the densities in Table 1. The green asterisk indicates the centroid of the CME, and the green line indicates its heliocentric distance. The black circle indicates the solar limb (radius $= 1R_{\odot}$).

source region for this CME was the active region AR12522 (N12W83) mentioned in Section 2.1. *STEREO-A* was at $\approx E163^{\circ}$ during the onset of the CME.¹⁰ The location of the active region therefore corresponds to $\approx 24^{\circ}$ behind the limb for the *STEREO-A* view.

The deprojected heliocentric distances of the CME were calculated for *STEREO-A/COR1* images by assuming that the projection effects vary as $1/\cos(\phi)$, where ϕ is the angle from the plane of sky and is equal to $\approx 24^{\circ}$ in the present case (see Table 1 for the deprojected r_{CME} at different epochs). Figure 4 shows *SDO/AIA* 211 Å observations of activity in the source region of the above CME. The evolution of a flux rope (marked with a blue line) and a diffuse shock ahead of it (marked with a yellow line), as described in Gopalswamy et al. (2012), can be clearly noticed. The leading edge (LE) of the flux rope (r_{fl}) and the shock (r_{sh}) are located at $\approx 1.06R_{\odot}$ and $\approx 1.13R_{\odot}$, respectively, at $\approx 06:36:36$ UT. The values of r_{fl} , r_{sh} , and the radius of curvature (r_c) of the flux rope at different epochs are listed in Table 2. Figure 5 shows the *SOHO/LASCO-C2* observations of the CME at $\approx 07:00$ UT, along with the *SDO/AIA* 211 Å and GRAPH observations at epochs earlier than the appearance of the CME in the *SOHO/LASCO-C2* FOV. It appears that the flux-rope structure in EUV, the type II radio burst, and the white-light CME are all closely associated. Note that the projection effects are very minimal in all the above three observations since AR12522 is almost at the limb of the Sun. We find that the shock is not noticeable in the *STEREO-A/COR1* white-light observations (see Figure 3). It is possible that the shock had become fainter by the time the CME reached the *STEREO-A/COR1* FOV.

3. Analysis and Results

3.1. Estimates of Coronal Electron Density (N_e)

3.1.1. Radio Imaging Observations with GRAPH

An inspection of Figure 5 indicates that the centroid of the type II burst (r_{radio}) observed with GRAPH at 80 MHz and 53.3

Table 1
Density Estimates Using *STEREO-A/COR1* Data

Time (UT)	Deprojected r_{CME}^a (R_{\odot})	Background Density ($\times 10^6 \text{ cm}^{-3}$)	CME Density ($\times 10^6 \text{ cm}^{-3}$)
06:50	1.82	7.34 ± 1.53	2.71 ± 2.46
06:55	2.00	4.32 ± 0.86	2.35 ± 1.56
07:00	2.06	3.49 ± 0.90	1.66 ± 1.17
07:05	2.24	2.21 ± 0.73	0.95 ± 0.91

Note.

^a Centroid of the CME.

MHz are located at $\approx 1.6 \pm 0.2R_{\odot}$ and $\approx 1.9 \pm 0.2R_{\odot}$, respectively. Any possible error in the position of the burst due to propagation effects such as scattering by density inhomogeneities in the solar corona and/or refraction in the Earth's ionosphere is expected to be within the above error limit (Stewart & McLean 1982; Ramesh et al. 1999b, 2006a, 2012b; Kathiravan et al. 2011; Mercier et al. 2015; Mugundhan et al. 2016, 2018). The fact that the Sun is presently in the phase of minimum activity (during which the observations reported in the present work were carried out) also indicates that the scattering will be less (Sasikumar Raja et al. 2016; Mugundhan et al. 2017). We calculated N_e at the above two heliocentric distances using the relation $N_e = \left(\frac{f_p}{9 \times 10^{-3}}\right)^2$, where f_p is the fundamental plasma frequency in units of MHz and N_e is in units of cm^{-3} . We would like to note here that the type II burst in the present case is mostly due to harmonic plasma emission ($2f_p$) since the locations of the bursts as observed with GRAPH at 80 and 53.3 MHz are above the limb (see Figure 5). The consistency of the estimated peak dcp of the bursts from the GRASP observations ($\approx 8\% - 11\%$; see Section 2.1) with those reported in the literature for harmonic plasma emission also indicate the same (see, for example, Dulk & Suzuki 1980). An inspection of the dynamic spectra of the type II burst as observed with GLOSS indicates the presence of a faint fundamental component of the type II burst at

¹⁰ https://stereo-ssc.nascom.nasa.gov/cgi-bin/make_where_gif

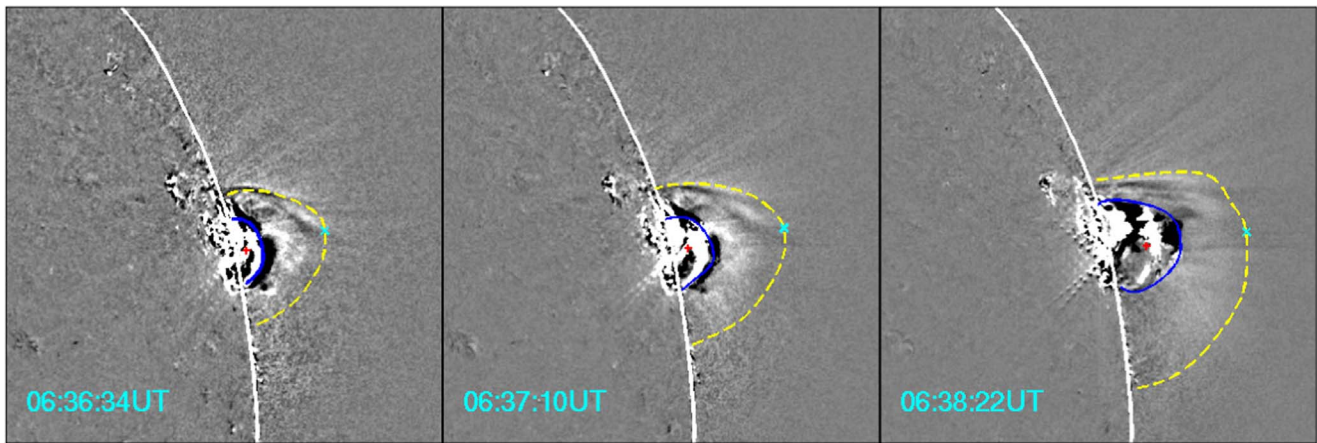


Figure 4. Evolution of the flux rope and shock in *SDO/AIA* 211 Å FOV near the source region of the CME in Figure 3. The white line indicates the solar limb (radius = $1R_{\odot}$). The blue and yellow markings indicate the flux-rope structure and shock ahead of it, respectively. The red plus marks correspond to the center of the hemispherical structure (assumed) for the flux rope. The cyan crosses represent the LE of the shock.

frequencies $\lesssim 50$ MHz.¹¹ These confirm that the type II bursts observed with GRASP (Figure 1) and GRAPH (Figure 5) are due to harmonic emission. So we substituted 40 and 26.7 MHz for f_p in the above relation, and obtained the values of N_e as $1.98 \times 10^7 \text{ cm}^{-3}$ at $\approx 1.6R_{\odot}$ ($f_p = 40$ MHz) and $8.77 \times 10^6 \text{ cm}^{-3}$ at $\approx 1.9R_{\odot}$ ($f_p = 26.7$ MHz).

3.1.2. White-light Observations with STEREO-A/COR1

The pB measurements with the *STEREO-A/COR1* were used to estimate the densities before the occurrence of the CME (i.e., the background corona at the location of the CME) and during the CME, at different heliocentric distances. The difference images used for this purpose were obtained using the observations of the CME at $\approx 06:50$ UT, 06:55 UT, 07:00 UT, and 07:05 UT, and that of the undisturbed background corona at $\approx 06:45$ UT (see Figure 3). Table 1 provides the CME-related details obtained from the aforementioned difference images. The deprojected r_{CME} at the above epochs are listed in column 2 of Table 1. Note that we had multiplied the measured projected values of r_{CME} by $1/\cos(24^\circ)$ to remove the projection effects (see Section 2.2). The N_e values of the undisturbed background corona and the CME at the corresponding heliocentric distances are listed in columns 3 and 4 of Table 1. The densities were calculated using the spherically symmetrical inversion technique (Wang & Davila 2014). Note the aforementioned densities correspond to the average density inside the region enclosed by the red box in the lower panels of Figure 3.

Figure 6 shows the plot of the N_e values obtained using GRAPH and *STEREO-A/COR1* observations as mentioned above. The error in the density estimates from *STEREO-A/COR1* is chiefly due to the errors associated with the instrumental background subtraction and the spherically symmetric approximation (Wang & Davila 2014; Wang 2017). The error in the density estimates from GRAPH is due to variation in N_e over the bandwidth of observations (≈ 2 MHz). The power-law fit to the data indicates that $N_e(r) = 2.3 \times 10^8 r^{-5.3}$ in the range $r \approx 1.6\text{--}2.2R_{\odot}$. Note that $N_e(r)$ varies typically as r^{-6} in the range $1.1 \lesssim r \lesssim 2.3R_{\odot}$ (Baumbach 1937). Considering this, and since we are interested

in understanding the characteristics of the CME close to the Sun also in the present case using the *SDO/AIA* 211 Å observations of the associated flux-rope structure (see Figure 4), we assumed that the above empirical relationship should be valid over $r \approx 1.1\text{--}2.2R_{\odot}$. We find that $N_e(r)$ estimated using the above relation for the *SDO/AIA* 211 Å observations in Figure 4 are reasonably consistent with the $N_e(r)$ values reported by Zucca et al. (2014a) in the same distance range ($r \approx 1.1\text{--}1.3R_{\odot}$) utilizing the emission measures derived from *SDO/AIA* observations for a similar flare associated CME/type II burst event.

3.2. Tracing the Path of the CME

Figure 7 shows the height–time (h – t) plot of the LE of the EUV flux-rope structure as observed with *SDO/AIA* 211 Å, locations of the type II bursts observed with GRAPH at 80 and 53.3 MHz and GRASP at two different frequencies in the range $\approx 90\text{--}50$ MHz, and the LE of the CME in the FOV of the *STEREO-A/COR1* coronagraph (see Figure 3) and *SOHO/LASCO-C2*. For the GRASP data in the plot we used two representative frequencies, viz. 82 and 50 MHz (in the lower band L of the harmonic emission; see Figure 1). Their heliocentric distances are $r \approx 1.58R_{\odot}$ and $1.93R_{\odot}$, respectively. Note that in the case of the GRASP observations, the locations of the type II bursts were estimated using the relationship between f_p and N_e , and the model for $N_e(r)$ derived in Section 3.1. The *SDO/AIA* 211 Å values are limited to less than $r \approx 1.23R_{\odot}$ and radio + white-light values are available only beyond $r \approx 1.58R_{\odot}$. So we used two separate quadratic fits for the h – t data in Figure 7: one for the former with an acceleration of $\approx 1259 \text{ m s}^{-2}$, and the other for the latter with an acceleration of $\approx -46 \text{ m s}^{-2}$. The comparatively large acceleration in the *SDO/AIA* 211 Å FOV was during the onset-peak phase of the associated *GOES/SXR* flare (see Section 2.1). This is consistent with earlier reports of acceleration of the flux-rope structure in the *SDO/AIA* observations during the impulsive phase of the flare (see, for example, Zhang et al. 2012). The decrease in acceleration in the present case is during the decay phase of the flare. We find that there is reasonable consistency between the two quadratic fits in Figure 7. This is expected since the early signature of a CME close to the Sun is usually an expanding flux-rope structure (Pomoell et al. 2009; Ma et al. 2011; Gopalswamy et al.

¹¹ https://www.iiap.res.in/gauribidanur/GLOSS-dailyimages/Mar-2016/GBD_DSPEC_20160316.jpeg

Table 2
Estimates of B and the Related Parameters from *SDO/AIA* 211 Å Observations

Time (UT)	r_{sh} (R_{\odot})	r_{n} (R_{\odot})	r_c (R_{\odot})	Δr (R_{\odot})	δ	M_a	v_a (km s^{-1})	B (G)
06:36:34	1.12	1.04	0.025	0.083	3.35	1.12
06:37:10	1.15	1.06	0.035	0.090	2.59	1.15	401	1.93
06:37:46	1.17	1.08	0.040	0.101	2.50	1.16	400	1.83
06:38:22	1.19	1.10	0.046	0.095	2.06	1.19	390	1.74

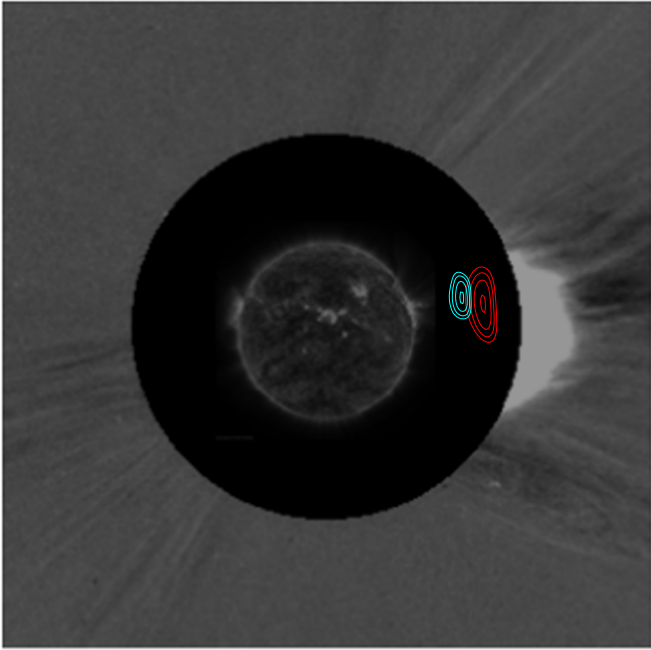


Figure 5. Locations of the type II bursts observed with the GRAPH on 2016 March 16 at 80 MHz ($\approx 06:47:15$ UT) and 53.3 MHz ($\approx 06:49:48$ UT) superposed on the *SDO/AIA* 211 Å image ($\approx 06:39:36$ UT), and the *SOHO/LASCO-C2* difference image ($\approx 07:00$ UT) obtained on the same day. Solar north is straight up, and east is to the left. The red and cyan color contours represent the GRAPH observations at 53.3 MHz and 80 MHz, respectively. The peak brightness temperatures (T_b) of the burst are $\approx 2.66 \times 10^8$ K (80 MHz) and $\approx 4.46 \times 10^8$ K (53.3 MHz). The radio contours shown are at 50%, 65%, 80%, and 99% of the peak T_b . The black circle indicates the occulting disk of the coronagraph. Its radius is $\approx 2.2R_{\odot}$. The bright patch of emission above the coronagraph occulter on its west corresponds to the CME mentioned in the text.

2012, 2013; Patsourakos & Vourlidis 2012; Cho et al. 2013), and CME-driven magnetohydrodynamic shocks generate type II bursts in the solar atmosphere (Mann et al. 1995; Aurass 1997; Claßen & Aurass 2002; Gopalswamy 2006; Cho et al. 2008; Vršnak & Cliver 2008; Gopalswamy et al. 2009; Ramesh et al. 2010a, 2012a; Kumari et al. 2017a). An estimate of the linear speed of the CME LE from the white-light data (*STEREO-A/COR1* and *SOHO/LASCO-C2*) in the range $r \approx 2.0$ – $5.0 R_{\odot}$ (see Figure 7) indicates it is $\approx 1000 \text{ km s}^{-1}$. The estimated shock speed ($v_s = v_a \times M_a$, where v_a is the Alfvén speed and M_a is the Mach number) for the type II burst is $\approx 825 \text{ km s}^{-1}$ (see Table 3). This is in good agreement with the speed of the CME LE. Note that though a shock was observed in the *SDO/AIA* 211 Å FOV, no type II burst was observed at that time. One likely reason for the absence of the type II burst could be the smaller values of M_a associated with the above shock (see Table 2). According to Mann et al. (2003) and Warmuth & Mann (2005), M_a should well exceed unity ($\gtrsim 1.4$) for the occurrence of a type II burst.

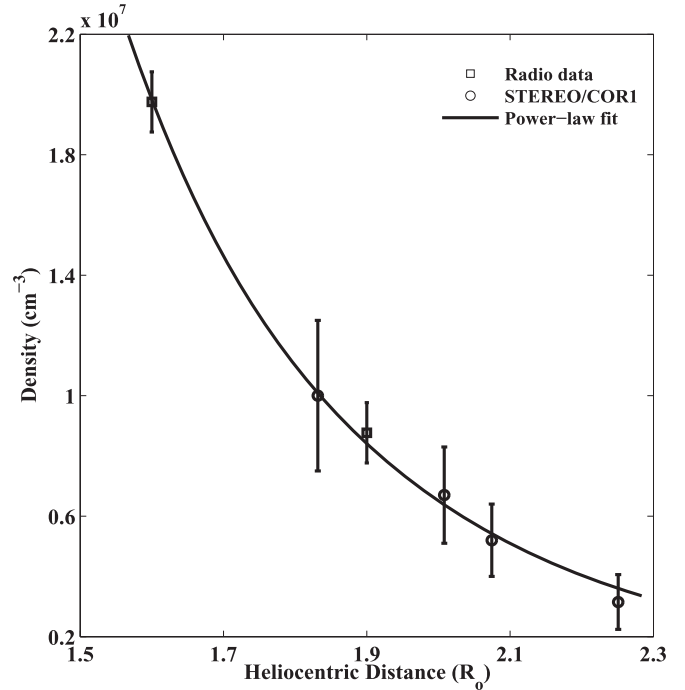


Figure 6. Density estimates from radio (GRAPH) and white-light (*STEREO-A/COR1*) observations. The solid line is a power-law fit ($N_e(r) = 2.3 \times 10^8 r^{-5.3}$) to the data.

3.3. Estimates of the Coronal Magnetic Field Strength (B)

Our aim is to directly estimate B using the observed data and with minimal assumptions. We used the following theoretical relation for this purpose:

$$B = \frac{v_a \times \sqrt{N_e}}{2.18 \times 10^6}, \quad (1)$$

where B is in units of G. We used the empirical relationship in Section 3.1 to obtain $N_e(r)$. The estimated values are in the range $\approx 1.39 \times 10^8$ – $3.6 \times 10^6 \text{ cm}^{-3}$ over $r \approx 1.10$ – $2.20 R_{\odot}$, the combined distance range of the *SDO/AIA* 211 Å and radio observations in the present case. M_a was estimated independently for the aforementioned two observations since they correspond to different heliocentric distance ranges.

3.3.1. *SDO/AIA* 211 Å Observations

Figure 4 shows the initial stages of the CME formation in the *SDO/AIA* 211 Å FOV in the present case. Measuring the locations and characteristics of the corresponding structures, i.e., the flux rope and the shock ahead of it, at different epochs helps to calculate M_a using the relation (see, for example,

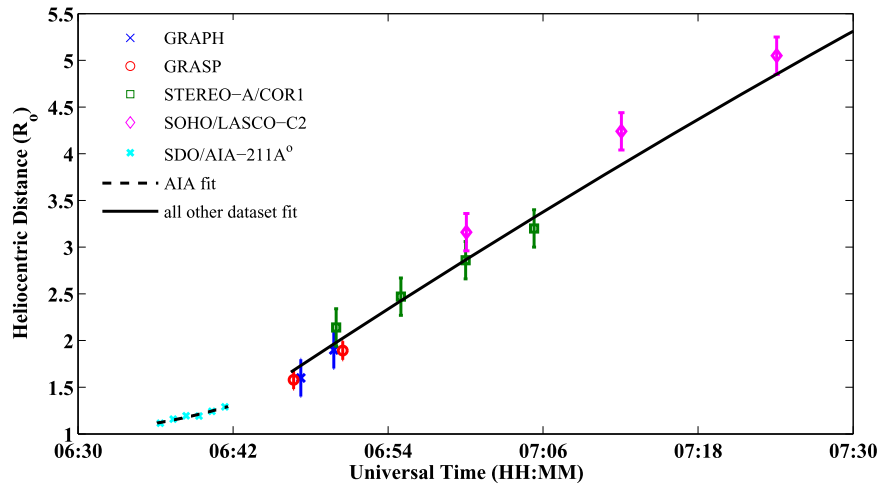


Figure 7. Height–time plot of the EUV shock (*SDO/AIA* 211 Å), type II radio bursts (GRAPH and GRASP), and the white-light CME (*STEREO-A/COR1* and *SOHO/LASCO-C2*). The dashed black line is a quadratic fit to *SDO/AIA* 211 Å data, and the solid black line is a quadratic fit to the GRAPH, GRASP, *STEREO-A/COR1*, and *SOHO/LASCO-C2* data.

Veronig et al. 2010; Gopalswamy et al. 2012)

$$M_a = \sqrt{1 + [1.24\delta - (\gamma - 1)/(\gamma + 1)]^{-1}}, \quad (2)$$

where δ is the relative standoff distance and γ is the adiabatic constant. The heliocentric distance of the shock (r_{sh}), LE of the CME flux rope (r_{fl}), thickness of the shock $\Delta r = r_{sh} - r_{fl}$, and radius of curvature (r_c) of the CME flux rope are used to calculate $\delta = \frac{\Delta r}{r_c}$. γ was assumed to be 4/3 for the present calculations (see Kumari et al. 2017b, 2017c for details). The different values estimated using Figure 4 are listed in columns 2–6 of Table 2. We then calculated v_s for the adjacent time intervals in column 1 using the values of r_{sh} in column 2. Finally, v_a values in column 8 were obtained using the relation $v_a = v_s/M_a$. We find that the location of the active region in the present work and that of the event reported in Gopalswamy et al. (2012) are nearly the same ($\approx W84$). Furthermore, the v_a values (≈ 400 – 500 km s $^{-1}$) and the angular width of the CME ($\approx 36^\circ$) are also reasonably close in the two cases. So, assuming 06:36:34 UT as the first appearance time (i.e., $t = 0$ of the flux rope and the shock in Figure 4), we independently calculated the corresponding r_{sh} , r_{fl} , and r_c values as a function of time using the empirical equations mentioned in Figures 3(a) and (b) of Gopalswamy et al. (2012). The constants in the aforementioned equations were replaced by the values of r_{sh} , r_{fl} , and r_c at 06:36:34 UT (see Table 2). Interestingly, the empirically calculated values agree well with the direct estimates.

3.3.2. Radio Spectral Observations with GRASP

For the radio observations, M_a was calculated using the following equation (Smerd et al. 1974; Mann et al. 1995; Vrřnak et al. 2002):

$$M_a = \sqrt{\frac{X(X + 5)}{2(4 - X)}}, \quad (3)$$

where X is density jump across the shock during the type II burst. The density jump is calculated from the instantaneous bandwidth (BDW) of the burst, i.e., $BDW = \frac{F_U - F_L}{F_L}$ and $X = (BDW + 1)^2$. F_U and F_L are the upper and lower

frequency components of the type II burst in the dynamic spectra. To estimate the B values, F_L is used as it corresponds to the undisturbed corona. Table 3 lists the different values estimated from the type II burst observations in Figure 1. The v_a values in column 8 were obtained in the same manner as the *SDO/AIA* 211 Å case described in Section 3.3.1, but Equation (3) was used for the calculations of M_a .

3.3.3. The Radial Variation of the Coronal Magnetic Field Strength

Figure 8 shows the B values estimated using the *SDO/AIA* 211 Å and GRASP observations. The respective estimates are consistent with each other, though they correspond to two different heliocentric distance ranges. A single power-law fit of the form $B(r) = 2.61 \times r^{-2.21}$ nicely describes the distribution. The only available two-dimensional magnetic field map obtained using coronal Zeeman magnetometry and full-Stokes spectropolarimetric measurements indicates that $B \approx 3.6$ G at $r \approx 1.1R_\odot$ (Lin et al. 2004). Compared to this, the present results predict $B \approx 2.1$ G at the same distance.

4. Summary

We have reported a CME, coronal type II radio burst, and flux-rope structure (in EUV) that were observed simultaneously on 2016 March 16. The radio burst was observed in both the imaging and spectral mode. The combined h – t plot indicates that all the three events are closely associated. We derived an empirical relation for the coronal electron density ($N_e(r) = 2.3 \times 10^8 r^{-5.3}$) using EUV observations of the flux-rope structure associated with the CME, spectral and imaging observations of the type II burst associated with the CME, and pB measurements of the corresponding white-light CME. Using the density values thus obtained along with the Alfvén Mach number (M_a) values from EUV and radio observations, we independently estimated the coronal magnetic field strength ($B(r)$). Our results indicate that $B(r) = 2.61 \times r^{-2.21}$ in the distance range $r \approx 1.1$ – $2.2R_\odot$. Mancuso & Garzelli (2013) had derived $B(r) = 3.76 \times r^{-2.29}$ in the distance range $r \approx 1.8$ – $14R_\odot$ by combining split-band type II observations and Faraday rotation measurements of extragalactic radio sources occulted by the solar corona. This is nearly same as the

Table 3
Estimates of B and the Related Parameters from GRASP Observations

Time (UT)	F_U (MHz)	F_L (MHz)	BDW	X	M_a	R (R_\odot)	v_a (km s^{-1})	B (G)
06:47:10	102.44	81.89	0.25	1.56	1.45	1.58	579	1.21
06:48:02	91.12	72.37	0.26	1.59	1.47	1.65	571	1.06
06:49:28	79.51	57.48	0.38	1.91	1.78	1.86	472	0.69
06:51:00	65.82	47.65	0.38	1.91	1.77	1.99	473	0.58
06:53:35	54.50	40.21	0.36	1.84	1.70	2.12	493	0.51
06:57:00	45.57	35.74	0.27	1.63	1.51	2.15	558	0.50

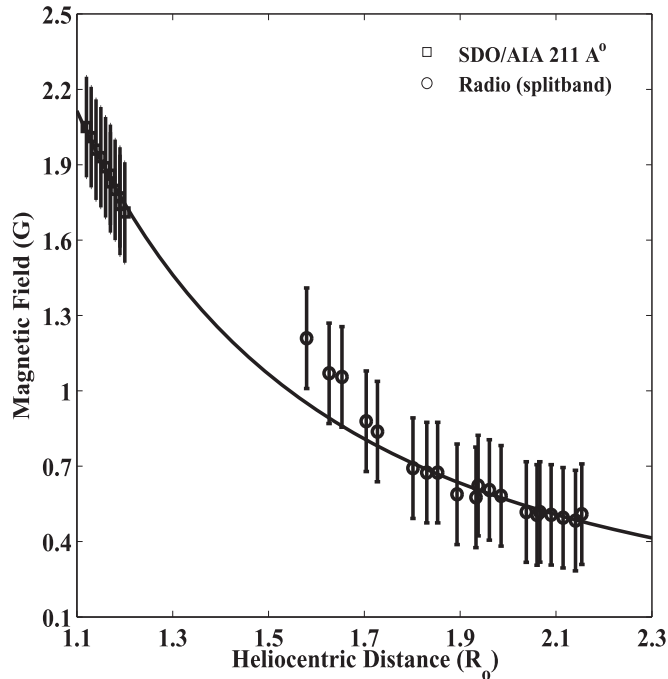


Figure 8. Estimates of B from SDO/AIA 211 Å and radio observations. The solid black line is a power-law fit ($B = 2.61 \times r^{-2.21}$) to the data points.

empirical relation for $B(r)$ in the present case. The present measurements are also in reasonable agreement with that reported by Lin et al. (2004) at $r \approx 1.1R_\odot$ using white-light observations. The consistency between the different measurements, though they correspond to different active regions observed at different epochs, strengthens the robustness of the estimates using radio observations. We expect that the density model-independent direct estimates of $B(r)$ reported in this work would lead to similar attempts in the future for unambiguous estimates of $B(r)$ in the region of the corona where white-light observations are presently difficult.

We would like to thank the staff of the Gauribidanur observatory for their help in maintenance of the antenna receiver systems and the observations. The work of T.J.W. was supported by NASA Cooperative Agreement NNG11PL10A to CUA and NASA grants 80NSSC18K1131 and 80NSSC18K0668. N.G. was supported in part by NASA's Living With a Star program. A.K. acknowledges V. Mugundhan and Vaibhav Pant for discussions. The *SOHO* data are produced by a consortium of the Naval Research Laboratory (USA), Max-Planck-Institut fuer Aeronomie (Germany), Laboratoire d'Astronomie (France), and the University of Birmingham (UK). *SOHO* is a project of international

cooperation between ESA and NASA. The *SOHO-LASCO* CME catalog is generated and maintained at the CDAW Data Center by NASA and the Catholic University of America in cooperation with the Naval Research Laboratory. The *SDO/AIA* data are courtesy of the NASA/*SDO* and the AIA science teams. We thank the referee for an insightful report that helped us improve the paper substantially.

ORCID iDs

Anshu Kumari <https://orcid.org/0000-0001-5742-9033>
T. J. Wang <https://orcid.org/0000-0003-0053-1146>
N. Gopalswamy <https://orcid.org/0000-0001-5894-9954>

References

- Aurass, H. 1997, in *Coronal Physics from Radio and Space Observations*, ed. G. Trotter (Berlin: Springer), 135
- Bastian, T. S., Pick, M., Kerdran, A., Maia, D., & Vourlidas, A. 2001, *ApJL*, 558, L65
- Baumbach, S. 1937, *AN*, 263, 121
- Benz, A. O., Monstein, C., Meyer, H., et al. 2009, *EM&P*, 104, 277
- Breckner, G. E., Howard, R. A., Koomen, M. J., et al. 1995, *SoPh*, 162, 357
- Cho, K.-S., Bong, S.-C., Kim, Y.-H., Moon, Y.-J., et al. 2008, *A&A*, 491, 873
- Cho, K.-S., Gopalswamy, N., Kwon, R.-Y., Kim, R.-S., & Yashiro, S. 2013, *ApJ*, 765, 148
- Cho, K.-S., Lee, J., Gary, D. E., Moon, Y.-J., & Park, Y.-D. 2007, *ApJ*, 665, 799
- Claßen, H. T., & Aurass, H. 2002, *A&A*, 384, 1098
- Dulk, G. A., & McLean, D. J. 1978, *SoPh*, 57, 279
- Dulk, G. A., & Suzuki, S. 1980, *A&A*, 88, 203
- Ebenezer, E., Ramesh, R., Subramanian, K. R., Sundara Rajan, M. S., & Sastry, C. V. 2001, *A&A*, 367, 1112
- Ebenezer, E., Subramanian, K. R., Ramesh, R., Sundara Rajan, M. S., & Kathiravan, C. 2007, *BASI*, 35, 111
- Gopalswamy, N. 2006, *GMS*, 165, 207
- Gopalswamy, N., Nitta, N., Akiyama, S., Mäkelä, P., & Yashiro, S. 2012, *ApJ*, 744, 72
- Gopalswamy, N., Thejappa, G., Sastry, C. V., & Tlamicha, A. 1986, *BAICz*, 37, 115
- Gopalswamy, N., Thompson, W. T., Davila, J. M., et al. 2009, *SoPh*, 259, 227
- Gopalswamy, N., Xie, H., Mäkelä, P., Yashiro, S., & Akiyama, S. 2013, *AdSpR*, 51, 1981
- Hariharan, K., Ramesh, R., & Kathiravan, C. 2015, *SoPh*, 290, 2479
- Hariharan, K., Ramesh, R., Kishore, P., Kathiravan, C., & Gopalswamy, N. 2014, *ApJ*, 795, 14
- Howard, R. A., Moses, J. D., Vourlidas, A., et al. 2008, *SSRv*, 136, 67
- Kathiravan, C., Ramesh, R., Barve, I. V., & Rajalingam, M. 2011, *ApJ*, 730, 91
- Kishore, P., Kathiravan, C., Ramesh, R., & Ebenezer, E. 2017, *JApA*, 38, 24
- Kishore, P., Kathiravan, C., Ramesh, R., Rajalingam, M., & Barve, I. V. 2014, *SoPh*, 289, 3995
- Kishore, P., Ramesh, R., Hariharan, K., Kathiravan, C., & Gopalswamy, N. 2016, *ApJ*, 832, 59
- Kishore, P., Ramesh, R., Kathiravan, C., & Rajalingam, M. 2015, *SoPh*, 290, 2409
- Kumari, A., Ramesh, R., Kathiravan, C., & Gopalswamy, N. 2017a, *ApJ*, 843, 10
- Kumari, A., Ramesh, R., Kathiravan, C., & Wang, T. J. 2017b, *SoPh*, 292, 161
- Kumari, A., Ramesh, R., Kathiravan, C., & Wang, T. J. 2017c, *SoPh*, 292, 177
- Kwon, R.-Y., Kramar, M., Wang, T. J., et al. 2013, *ApJ*, 776, 55

- Lemen, J. R., Title, A. M., Akin, D. J., et al. 2012, *SoPh*, **275**, 17
- Lin, H., Kuhn, J. R., & Coulter, R. 2004, *ApJL*, **613**, L177
- Lin, H., Penn, M. J., & Tomczyk, S. 2000, *ApJL*, **541**, L83
- Ma, S., Raymond, J. C., Golub, L., et al. 2011, *ApJ*, **738**, 160
- Mancuso, S., Frassati, F., Bemporad, A., & Barghini, D. 2019, *A&A*, **624**, L2
- Mancuso, S., & Garzelli, M. V. 2013, *A&A*, **560**, L1
- Mancuso, S., Raymond, J. C., Kohl, J., et al. 2003, *A&A*, **400**, 347
- Mann, G., Classen, T., & Aurass, H. 1995, *A&A*, **295**, 775
- Mann, G., Klassen, A., Aurass, H., & Classen, H.-T. 2003, *A&A*, **400**, 329
- Mercier, C., Subramanian, P., Chambe, G., & Janardhan, P. 2015, *A&A*, **576**, 136
- Monstein, C., Ramesh, R., & Kathiravan, C. 2007, *BASI*, **35**, 473
- Mugundhan, V., Hariharan, K., & Ramesh, R. 2017, *SoPh*, **292**, 155
- Mugundhan, V., Ramesh, R., Barve, I. V., et al. 2016, *ApJ*, **831**, 154
- Mugundhan, V., Ramesh, R., Kathiravan, C., et al. 2018, *ApJL*, **855**, L8
- Patsourakos, S., & Vourlidas, A. 2012, *SoPh*, **281**, 187
- Pomoell, J., Vainio, R., & Pohjolainen, S. 2009, in Proc. IAU Symp. 257, Universal Heliophysical Processes, ed. N. Gopalswamy & D. F. Webb (Cambridge: Cambridge Univ. Press), 493
- Ramesh, R. 2011, in ASI Conf. 2, First Asia-Pacific Solar Physics Meeting, ed. A. R. Choudhuri & D. Banerjee (Bengaluru: ASI), 55
- Ramesh, R., Anna Lakshmi, M., Kathiravan, C., Gopalswamy, N., & Umapathy, S. 2012a, *ApJ*, **752**, 107
- Ramesh, R., Kathiravan, C., Barve, I. V., & Rajalingam, M. 2012b, *ApJ*, **744**, 165
- Ramesh, R., Kathiravan, C., Kartha, S. S., & Gopalswamy, N. 2010a, *ApJ*, **712**, 188
- Ramesh, R., Kathiravan, C., & Sastry, C. V. 2010b, *ApJ*, **711**, 1029
- Ramesh, R., Kathiravan, C., & Satya Narayanan, A. 2004, *AsJPh*, **13**, 277
- Ramesh, R., Kathiravan, C., & Satya Narayanan, A. 2011, *ApJ*, **734**, 39
- Ramesh, R., Kathiravan, C., Satya Narayanan, A., & Ebenezer, E. 2003, *A&A*, **400**, 753
- Ramesh, R., Kathiravan, C., Sundara Rajan, M. S., Barve, I. V., & Sastry, C. V. 2008, *SoPh*, **253**, 319
- Ramesh, R., Kishore, P., Mulay, S. M., et al. 2013, *ApJ*, **778**, 30
- Ramesh, R., Nataraj, H. S., Kathiravan, C., & Sastry, C. V. 2006a, *ApJ*, **648**, 707
- Ramesh, R., Subramanian, K., Sundara Rajan, M., & Sastry, C. V. 1998, *SoPh*, **181**, 439
- Ramesh, R., Subramanian, K. R., & Sastry, C. V. 1999a, *A&AS*, **139**, 179
- Ramesh, R., Subramanian, K. R., & Sastry, C. V. 1999b, *SoPh*, **185**, 77
- Ramesh, R., Sundara Rajan, M. S., & Sastry, C. V. 2006b, *ExA*, **21**, 31
- Sasikumar Raja, K., Ingale, M., Ramesh, R., et al. 2016, *JGRA*, **121**, 11605
- Sasikumar Raja, K., Kathiravan, C., Ramesh, R., Rajalingam, M., & Barve, I. V. 2013a, *ApJS*, **207**, 2
- Sasikumar Raja, K., & Ramesh, R. 2013b, *ApJ*, **775**, 38
- Sasikumar Raja, K., Ramesh, R., Hariharan, K., Kathiravan, C., & Wang, T. J. 2014, *ApJ*, **796**, 56
- Sastry, C. V. 2009, *ApJ*, **697**, 1934
- Smerd, S. F., Sheridan, K. V., & Stewart, R. T. 1974, in Proc. IAU Symp. 57, Coronal Disturbances, ed. G. A. Newkirk (Cambridge: Cambridge Univ. Press), 389
- Smerd, S. F., Sheridan, K. V., & Stewart, R. T. 1975, *ApL*, **16**, 23
- Stewart, R. T., & McLean, D. J. 1982, *PASAJ*, **4**, 386
- Tomczyk, S., Card, G. L., Darnell, T., et al. 2008, *SoPh*, **247**, 411
- Tun, S. D., & Vourlidas, A. 2013, *ApJ*, **766**, 130
- Veronig, A. M., Muhr, N., Kienreich, I. W., Temmer, M., & Vršnak, B. 2010, *ApJL*, **716**, L57
- Vršnak, B., & Cliver, E. W. 2008, *SoPh*, **253**, 215
- Vršnak, B., Magdalenic, J., Aurass, H., & Mann, G. 2002, *A&A*, **396**, 673
- Wang, T., & Davila, J. M. 2014, *SoPh*, **289**, 3723
- Wang, T., Reginald, N. L., Davila, J. M., Cyr, O. C., St., & Thompson, W. T. 2017, *SoPh*, **292**, 97
- Warmuth, A., & Mann, G. 2005, *A&A*, **435**, 1123
- Wiegelmann, T., Petrie, G. J. D., & Riley, P. 2017, *SSRv*, **210**, 249
- Zhang, J., Cheng, X., & Ding, M. 2012, *NatCo*, **3**, 747
- Zimovets, I., Vilmer, N., Chian, A. C.-L., Sharykin, I., & Struminsky, A. 2012, *A&A*, **547**, A6
- Zucca, P., Carley, E. P., Bloomfield, D. S., & Gallagher, P. T. 2014a, *A&A*, **564**, A47
- Zucca, P., Pick, M., Demoulin, P., et al. 2014b, *ApJ*, **795**, 68